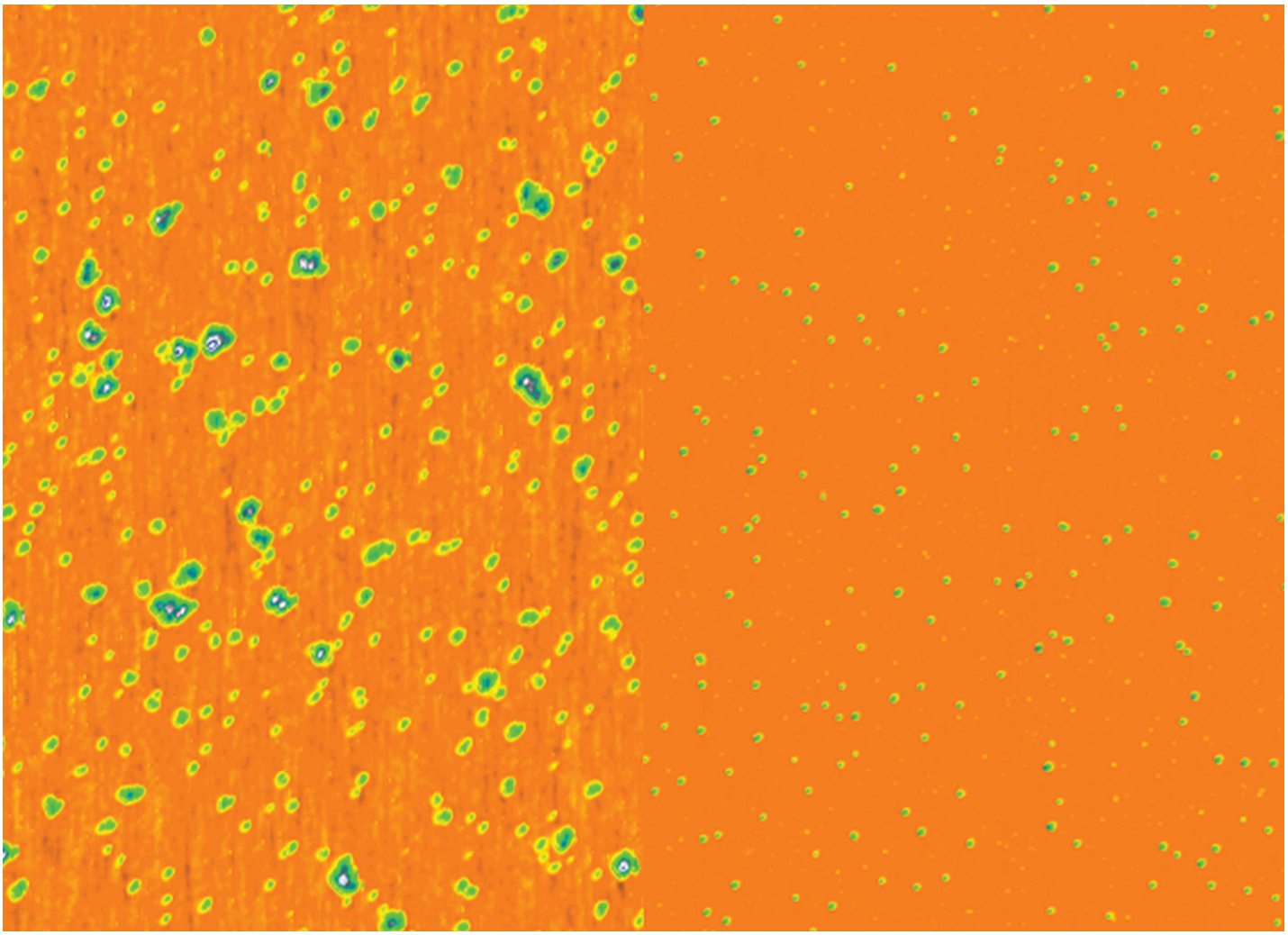

Highlighting work from the Liu Research Group at the National Institute of Standards and Technology Center for Neutron Research (NCNR) and University of Delaware.

Nanoparticle separation based on size-dependent aggregation of nanoparticles due to the critical Casimir effect

The nanoparticle aggregation induced by the critical Casmir interaction was observed to be very sensitive to the relative size of the nanoparticles. Due to the ubiquity of the critical Casmir interaction, this process leads to a very efficient and versatile method to separate nanoparticles based on their sizes.

As featured in:

See Yun Liu *et al.*, *Soft Matter*, 2018, **14**, 1311.

ROYAL SOCIETY OF CHEMISTRY

rsc.li/soft-matter-journal

Registered charity number: 207890

Soft Matter

PAPER

View Article Online
View Journal | View Issue

Cite this: *Soft Matter*, 2018, **14**, 1311

Nanoparticle separation based on size-dependent aggregation of nanoparticles due to the critical Casimir effect†

Hongyu Guo,[ab] Gheorghe Stan[c] and Yun Liu *[abd]

Nanoparticles typically have an inherent wide size distribution that may affect the performance and reliability of many nanomaterials. Because the synthesis and purification of nanoparticles with desirable sizes are crucial to the applications of nanoparticles in various fields including medicine, biology, health care, and energy, there is a great need to search for more efficient and generic methods for size-selective nanoparticle purification/separation. Here we propose and conclusively demonstrate the effectiveness of a size-selective particle purification/separation method based on the critical Casimir force. The critical Casimir force is a generic interaction between colloidal particles near the solvent critical point and has been extensively studied in the past several decades due to its importance in reversibly controlling the aggregation and stability of colloidal particles. Combining multiple experimental techniques, we found that the critical Casimir force-induced aggregation depends on relative particle sizes in a system with larger ones aggregating first and the smaller ones remaining in solution. Based on this observation, a new size-dependent nanoparticle purification/separation method is proposed and demonstrated to be very efficient in purifying commercial silica nanoparticles in the lutidine/water binary solvent. Due to the ubiquity of the critical Casimir force for many colloidal particles in binary solvents, this method might be applicable to many types of colloidal particles.

Received 2nd October 2017,
Accepted 24th December 2017

DOI: 10.1039/c7sm01971h

rsc.li/soft-matter-journal

1. Introduction

Since first discussed theoretically by Fisher and de Gennes in 1978,[1] the generic effective interaction between colloidal particles near the critical point of a solvent[2–4] has been widely investigated in binary solvents at both critical and off-critical solvent concentrations.[3,5] This effective colloidal interaction was found to be responsible for the stability of reversible particle aggregations[4,6–9] and can be tuned by controlling the relative compositions of a binary solvent and the temperature difference away from the demixing temperature of the solvent,[4,8–10] making it a promising method for colloidal assembly.[10] Even though different views of this effective interaction exist in the literature,[11–14] it has been widely termed as the critical Casimir force (CCF) since the 1990s.[11] The CCF-induced reversible aggregations have been studied in the past several decades, but the competition of particles with different sizes commonly present in almost all real systems with a varying degree of size polydispersity has not been investigated.

Here, we show conclusive experimental evidence that by controlling the CCF in the vicinity of the critical point of a binary solvent, we can regulate systematically the aggregation of colloidal particles based on particle sizes. For colloidal particles with different sizes suspended in near-critical binary liquid mixtures, we found that the formation of aggregates depends on the particle size at a given temperature. Larger particles tend to aggregate first and precipitate out of the suspension. At the same time, smaller particles tend to stay inside supernatants. The observation of this size-selective aggregation mechanism has never been reported before, and it offers new physics insights into the interesting reversible aggregations induced by the CCF. We further designed a novel particle purification/separation method based on the observed size-sensitive aggregation effect and demonstrated the efficiency of this method on widely studied colloidal silica nanoparticles (NPs).

It is important to point out that the properties and applications of nanoparticles strongly depend on their sizes and size distributions,[15–18] which in turn make the synthesis and preparation of NPs with desirable sizes and good monodispersity critical

[a] *Center for Neutron Research, National Institute of Standards and Technology, Gaithersburg, Maryland 20899, USA. E-mail: yunliu@nist.gov*
[b] *Department of Chemical and Biomolecular Engineering, University of Delaware, Newark, Delaware 19716, USA*
[c] *Materials Measurement Science Division, National Institute of Standards and Technology, Gaithersburg, Maryland 20899, USA*
[d] *Department of Physics and Astronomy, University of Delaware, Newark, Delaware 19716, USA*

† Electronic supplementary information (ESI) available. See DOI: 10.1039/c7sm01971h

for fundamental studies and applications in nanoscience.[19–21] Because impurities and large size distributions of NP products are still inevitable for many synthesis methods, the post-synthesis purification and size separation of NPs are of extreme importance. Recently, methods relying on size-dependent aggregation and self-assembly have been developed by introducing a tunable interaction between NPs, such as coating the NPs' surfaces,[22] adding salts and surfactants,[23–25] adding small depletion particles,[20] *etc.* Our method using the CCF adds a new method to the NP purification methods based on a generic interaction related to the critical phenomenon. Due to the universality of the involved critical phenomenon, this method may be applicable for a wide range of NPs and can be instrumental in tailoring their nanoscale properties and applications.

2. Materials and methods

P1 NPs (Ludox SM-30), P2 NPs (Ludox TM-50), and 2,6-dimethylpyridine (lutidine) (>99%) were purchased from Sigma-Aldrich and were used without any further treatment. D_2O (>99.9%) was purchased from Cambridge Isotope. Milli-Q water (18.2 MΩ cm) was used as H_2O in the preparation of all samples. Dynamic light scattering was performed with a DynaPro NanoStar M3300 instrument (Wyatt Technology Corp., Santa Barbara, CA). Atomic force microscopy was performed with a Bruker MultiMode 8 AFM (Bruker, Santa Barbara, CA) operated in intermittent scanning mode. Small-angle neutron scattering (SANS) was conducted on NG7-SANS, NGB 30m SANS, and nSoft 10m SANS instruments in the NIST Center for Neutron Research (see the ESI† for more details).

To study the particle size effects during the aggregation induced by the CCF and demonstrate the effectiveness of our new particle purification method, especially the purification of NPs in aqueous solutions, we have chosen a model system consisting of commercial silica NPs and a well-studied binary solvent, namely a 2,6-lutidine/water mixture. Water in this binary solvent allows various NPs with hydrophilic surfaces to be dispersed in this solvent. The 2,6-lutidine/H_2O mixture has the lower critical solution temperature T_c = 33.4 °C and the critical lutidine mole concentration at w_c = 0.0643.[26,27] (This molar concentration corresponds to 29% mass fraction of the lutidine and H_2O mixture. For some samples, we also prepared the solvent by mixing a different ratio of H_2O and D_2O, which may slightly shift the critical point. However, as detailed in the ESI,† this does not affect our experimental conclusions.)

Two samples with two commercial silica NPs, P1 and P2, were prepared. The size distributions of P1 and P2 NPs were measured by atomic force microscopy (AFM). The results indicate that the radii of the P1 and P2 NPs have the main modes at 5.0 nm and 13.1 nm, respectively, with the P1 NPs having a rather large particle size distribution (see the ESI† for details). Sample 1 was prepared with 0.4% volume fraction of P1 NPs only, and Sample 2 was prepared with 0.4% volume fraction of P1 NPs and 0.1% volume fraction of P2 NPs. The introduction of large P2 particles into the P1 particle solution for Sample 2 was to artificially increase size polydispersity by adding large particles.

3. Results and discussion

The general phase diagram of model binary solvent systems with dilute particle solutions has been extensively studied[7,28] and is shown schematically in Fig. 1. Note that the location of the aggregation phase depends on the surface properties of NPs and the properties of the binary solvent. Our silica NPs dispersed in this lutidine/water binary solvent favor the adsorption of water instead of lutidine on their surfaces (see the ESI† for details). Thus, reversible aggregates induced by the CCF are formed at the lutidine concentration, w, larger than w_c for relatively dilute particle conditions. Three different phases are emphasized: (1) the clear solution (1-phase) at either $w < w_c$ and temperatures below the binodal phase separation curve ($T_s(w)$, the solid line in Fig. 1) of the solvent or $w > w_c$ and $T < T_a(w)$ (the dashed line in Fig. 1), where $T_a(w)$ is the lowest temperature at which we observed precipitated aggregates at the bottom of the vial; (2) the turbid supernatant solution with some precipitated aggregates (1-phase with aggregations) in a narrow temperature range $T_a(w) < T < T_s(w)$ where $w > w_c$; and (3) the two-phase region of the solvent (2-phase) at

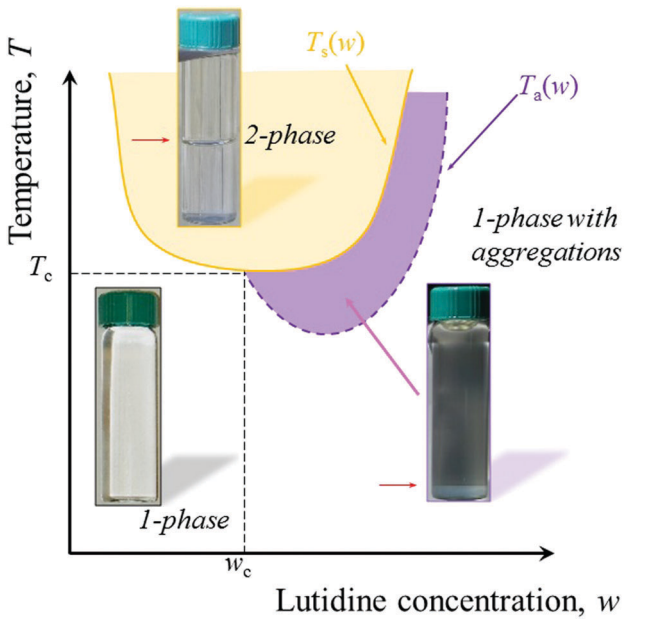

Fig. 1 Schematic picture of the general phase diagram of colloidal NPs suspended in lutidine/water mixtures. The solid curve $T_s(w)$ is the binodal phase separation line of pure 2,6-lutidine/water mixtures. T_c is the critical temperature and w_c is the critical concentration of lutidine. The dashed curve, $T_a(w)$, is the incipient temperature of samples with NP precipitates in solutions at $w > w_c$. The inserted pictures are typical examples of the samples at different phases: the clear solution (1-phase) at low temperatures, the turbid supernatant solution with some precipitates at $T_a(w) < T < T_s(w)$ and $w > w_c$ (1-phase with aggregations), and the phase separated solvent (2-phase, where lutidine is at the top and water with NPs is at the bottom) above the binodal curve of the solvent. The short red arrows indicate separations between different phases.

$T > T_s(w)$, where water and lutidine form two separated phases. Photos of one sample at these three phases are also shown in Fig. 1.

3.1 Size-sensitive nanoparticle aggregations

To observe the effect of particle size on aggregations, samples were studied in both the 1-phase region and the 1-phase with aggregations region as shown in Fig. 1. Both Sample 1 and Sample 2 were prepared with the mole concentration of lutidine w = 0.0899, which corresponds to 37% mass fraction for the lutidine/H_2O mixture. At room temperature, both samples are in the 1-phase region. And at a temperature around 28.9 °C, they enter the 1-phase with aggregations region. (Experiments on other lutidine concentrations also showed similar results.)

Small-angle neutron scattering (SANS) was used to study *in situ* the evolution of the size distributions of NPs suspended in solutions. Because large aggregates are heavier and thus can precipitate out of a neutron beam without centrifuging the samples, SANS was used to measure the particle concentrations and size distributions inside the supernatant. In comparison with the initial particle concentration and size distribution, information regarding particles in the precipitated aggregates can be obtained. In addition, taking advantage of the contrast variation technique[29] by mixing D_2O and H_2O (the mole ratio between D_2O and H_2O, M_{D_2O}/M_{H_2O}, is 0.328) to match the scattering length density (SLD) of lutidine, the contribution from the solvent density fluctuation to SANS signals becomes negligible. Hence, the coherent scattering signals of SANS patterns are only from NPs in solutions (see the ESI† for details).

SANS data are very sensitive to the particle size distribution. This is illustrated in Fig. 2 by the scattering patterns of three samples: (1) 0.4% volume fraction of P1 particles (red circles), (2) 0.1% volume fraction of P2 particles (blue squares), and (3) the sample with both 0.4% volume fraction of P1 and 0.1% volume fraction of P2 (black triangles). Because P2 particles are larger, the SANS pattern from the P2 sample decays faster as the scattering wave vector, Q, increases, while the signal from the P1 sample decays much slower because the particles are smaller. This characteristic response as a function of Q is a powerful indicator for the size distribution of NPs studied by SANS. The signal from the P1–P2 mixture is simply the sum of the coherent signals from the P1 and P2 samples. (Note that there is a constant incoherent scattering background from the solvent. In the ESI,† these SANS curves are also plotted by shifting different curves vertically to show some details of each SANS curve.)

Fig. 3A shows SANS scattering patterns of Sample 1 at a few temperatures from the 1-phase region to the 1-phase with aggregations region. The variation of the SANS patterns as a function of the temperature indicates a large change in particle concentration and size distribution in the supernatant. To quantitatively analyze the SANS data, the size distribution of Sample 1 was modelled as two populations of spherical NPs, whose size distributions are approximated by the Schultz distributions.[30] The first population, P1-p, represents small particles with a particle size of around 5 nm in radius as shown later by our AFM results. The second population, P1-i, represents the impurity particles which have larger sizes with a broad distribution; such a distribution was confirmed by the AFM measurement. For each population of NPs, the Schultz distribution has two characteristic parameters, the mean radius R and width σ_R.[30] Hence, the fitting parameters of each population are the volume fraction φ, the mean radius R, and the polydispersity index $f \equiv \sigma_R/R$ (see the ESI† for details). The fitting curves are shown as the solid lines in Fig. 3A.

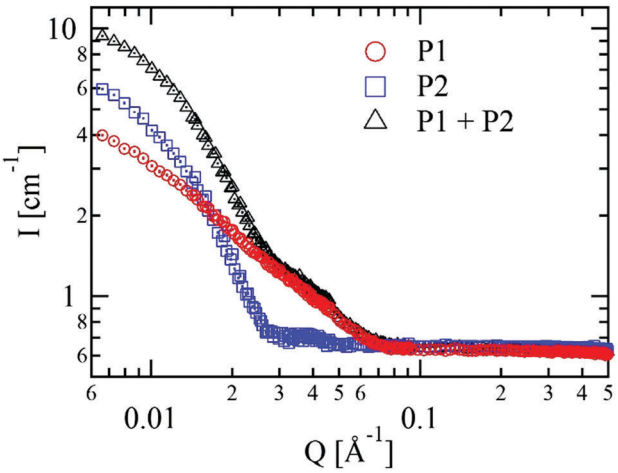

Fig. 2 Small-angle neutron scattering data of three different NP samples measured at room temperature. 0.4% volume fraction of P1 NPs (red circles), 0.1% volume fraction of P2 NPs (blue squares), and the mixture of P1 (0.4% volume fraction) and P2 (0.1% volume fraction) NPs (black triangles) are dispersed in the matched lutidine/water solvents with w = 0.0899 (corresponding to 37% mass fraction for the lutidine/H_2O mixture). The error bars represent one standard deviation (SD) and are smaller than the symbols. Each curve contains 220 data points.

The extracted values of φ and R for P1-p and P1-i at different T values are shown in Fig. 3B and C, respectively. Note that when NPs form aggregates, some precipitate out of the solution while some smaller aggregates remain in the supernatant. The effects of the aggregates in the supernatant are included in P1-i because the aggregate size is much bigger than P1-p. At $T < T_a$, the size and volume fraction for both P1-p and P1-i show no changes as no particles aggregate and precipitate out of the solution. At $T > T_a$, there is a dramatic decrease of φ for P1-i, which indicates the removal of large particles due to precipitation. (Note that R increases substantially for P1-i due to aggregation at $T > T_a$.) At T = 29.6 °C, there are only less than 2.5% of original impurities (P1-i) left in the solution, while more than 44% of original P1-p particles is still in solution based on the change in particle volume fractions. It is noted that at the highest temperature, even though the monodispersity of NPs becomes much better, we could not observe the high-Q oscillations of the form factor due to the high incoherent background.

These striking results indicate that there are significantly fewer large particles in the supernatant at high temperature in the 1-phase with aggregations region. Thus, the large particles preferentially participate in the aggregates and precipitate out of the solution. In other words, the CCF-induced aggregations

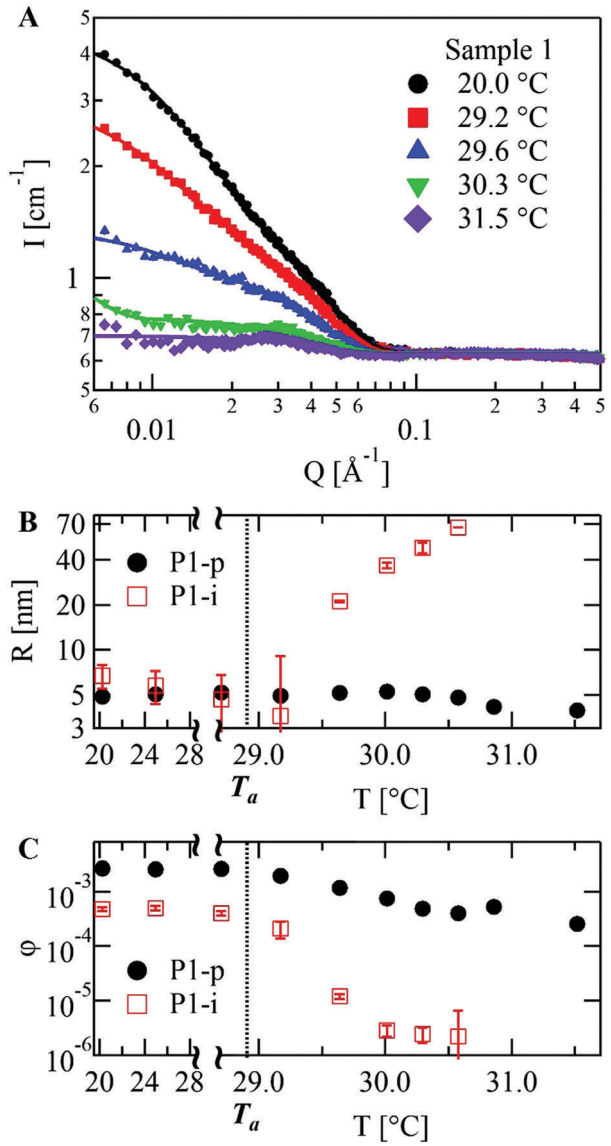

Fig. 3 *In situ* SANS studies of Sample 1: (A) SANS curves at different temperatures. Solid lines are fits to experimental data. (B) Fitting results of the particle sizes as a function of temperature. The vertical dotted line indicates T_a, which is the transition temperature of the observed precipitates in a solution. (C) Fitting results of the particle volume fractions as a function of temperature. The error bars represent one SD. Error bars may not be visible if they are smaller than symbols.

depend on the relative particle size. Note that the precipitates are reversible aggregates that can be dissolved by decreasing the temperature. As many colloidal particles have size polydispersity, the aggregation behavior might be affected by their size distributions.

This result also immediately implies that the CCF-induced aggregation can be applied to purify NPs based on their sizes. If we define the purity of the particles in the supernatant as the ratio between the volume fraction of P1-p and the total volume fraction of all particles in the supernatant, the purity improves to 99% from 85% by separating the CCF-induced precipitates at $T > 29.6$ °C. It is noted that at $T > 30.5$ °C, the particle radius of P1-p becomes smaller compared with the results obtained at lower temperatures. This is because the P1-p particles also have the size distribution and the larger particles in the original P1-p are now slowly separated from the rest of the P1-p population.

To further illustrate the particle size dependence of the CCF-induced aggregation, larger P2 particles were added into Sample 2. The *in situ* SANS studies of Sample 2 demonstrate similar results as shown in Fig. S4 in the ESI.† The large P2 particles preferentially participate in the aggregates and can be easily separated from the P1 particles. At $T = 29.6$ °C, there are more than 53% of the original P1-p NPs still in solution and the purity is above 95%. At $T = 30.3$ °C, there are still 21% of P1-p NPs in the solution and the purity is above 98.5%. The differences in yield rates and purities when compared with those of Sample 1 are attributed to the higher concentration of large-sized impurities of Sample 2 due to the addition of large P2 particles (see the ESI†).

It is noted that during the *in situ* experiment, the samples were allowed to wait about one hour before the data were collected. Even though the precipitation may take some time after each temperature change, the waiting time seems to be long enough to allow the precipitation process to be completed. Future experiments will be performed to understand the kinetic process of the precipitation.

3.2 Size-selective purification method based on the CCF

Based on the observation of the particle size-dependent aggregation induced by the CCF, we can devise a general nanoparticle purification method for the samples with a similar phase diagram as shown in Fig. 1 by the following procedure: (1) choose a lutidine composition for which the NP aggregation phase (1-phase with aggregations) can be reached by changing the temperature and prepare NP samples in the binary solvent at the 1-phase region. (2) Warm up the sample to a temperature T_p (the processing temperature) in the 1-phase with aggregations region to introduce precipitates. (3) The supernatant and precipitates are then separated and the supernatant contains the purified NPs. The size and polydispersity of the particles left in the supernatant sensitively depend on T_p, which are discussed in the rest of the paper. In our experiments, natural gravity is sufficient enough to cause large aggregates precipitating out of the solutions. Using a centrifuge can increase the precipitation rate and potentially increase the efficiency of our method that will be studied in future.

The temperature gap between $T_a(w)$ and $T_s(w)$ for a given lutidine mole concentration, w, determines the working temperature region for this NP purification method and is sensitive to the lutidine concentration. The transition boundary for $T_a(w)$ can be determined by visually observing the precipitates at the bottom of a vial by increasing the temperature. By further increasing the temperature to reach $T_s(w)$, the separation of two liquids (lutidine and water) can be observed by eye.

In our case, we have chosen $w = 0.0899$ due to the wide temperature region we can work with ($T_a(w) = 28.9$ °C and $T_s(w) = 32.7$ °C). (This mole ratio corresponds to 37% mass fraction of the lutidine/H_2O mixture.) The ratio of D_2O to H_2O is chosen to

be M_{D_2O}/M_{H_2O} = 0.328 so the experimental condition is consistent with the *in situ* SANS experiments. $T_a(w)$ is found to be very similar for Sample 1 and Sample 2. We applied this method to purify our silica nanoparticles in Sample 1 and Sample 2, and characterized the efficiency of purification at different processing temperatures T_p using dynamic light scattering (DLS), SANS, and AFM. It is worth pointing out that we have observed similar results at other lutidine concentrations too.

3.2.1 Characterization of purified nanoparticles using DLS and SANS. Purifications of Sample 1 and Sample 2 were conducted based on the aforementioned three steps at a few different T_p values. DLS and SANS were used to determine the average hydrodynamic radius, r_h, and the radius of gyration, r_g, of the purified NPs (see the ESI† for details). Both DLS and SANS measurements were performed at room temperature where the solutions were transparent. The scattering signals were dominated by silica NPs and had a negligible contribution from the solvent fluctuation. As shown in Fig. 4A and B, when T_p is below T_a, no significant particle size variations are observed by both DLS and SANS because silica NPs are stable (do not precipitate) in solutions at $T_p < T_a$ during the purification process. However, for $T_p > T_a$, the average radii of purified silica NPs as indicated by r_h and r_g decrease with the increase of T_p for both Sample 1 and Sample 2.

Fig. 4A and B also indicate that the average particle size decreases almost monotonically as a function of T_p when $T_p > T_a$. Thus, the average particle size of the purified sample can be finely and reversibly controlled by simply changing T_p. For Sample 2, despite the presence of a significantly larger amount of impurities (large particles from the introduction of P2 NPs) when compared with the impurity level in Sample 1, the average size of NPs after the purification reaches similar values of the purified Sample 1 at T_p = 29.7 °C. Therefore, our purification method is very efficient in removing large particles from each sample. The aggregation and precipitation processes are also schematically shown in Fig. 4C: the large particles (red balls) prefer to participate in the aggregation and by doing that they are separated from small particles (blue balls) by the precipitation.

3.2.2 Characterization of purified nanoparticles using AFM. To capture a more accurate characterization of the particle size distributions before and after purification, we resorted to AFM measurements of NPs dispersed at room temperature on freshly-cleaved mica surfaces (see the ESI† for details). Fig. 5 shows the representative histograms of the volume distribution of NPs as a function of particle size before the purification at T_p = 20 °C and after the purification at T_p = 31 °C. The total volume of all particles was normalized to one in Fig. 5A and B. (Note that the volume fraction of NPs is a very important parameter for the macroscopic properties of many NP-based materials.[31] Therefore, the histograms of the volume distribution are shown here instead of number distribution.) Measurements of both samples were collected at five different locations on the mica substrates deposited with silica NPs. The details of the AFM experiment are given in the ESI.†

As can be observed in Fig. 5A, the main mode of the particle size distribution of Sample 1 before purification at T_p = 20 °C

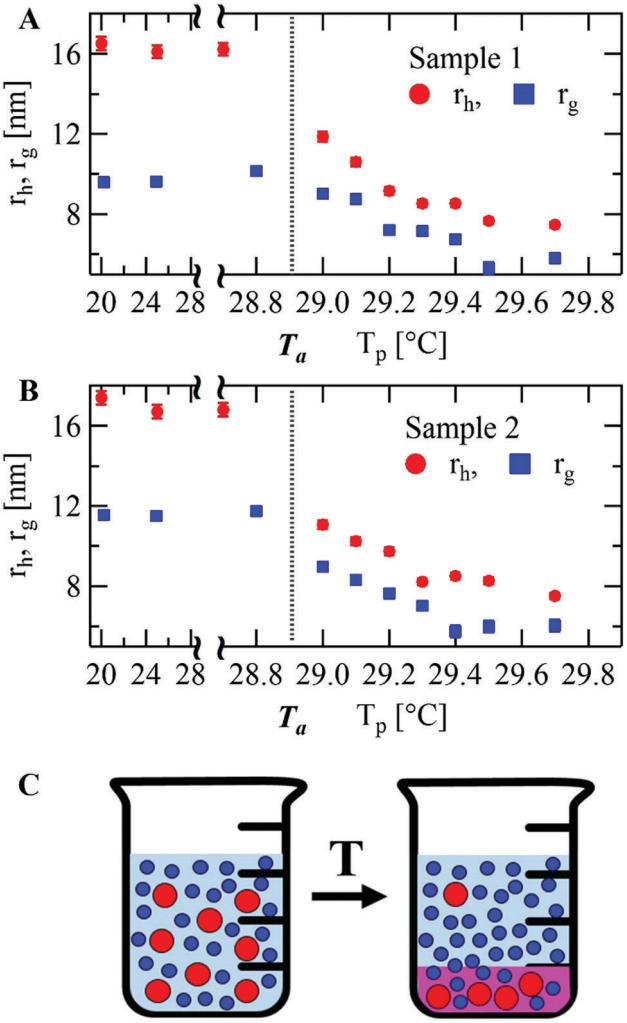

Fig. 4 The average hydrodynamic radius, r_h, and the radius of gyration, r_g, of the NPs after purification. The results are obtained by DLS and SANS. (A) Results of Sample 1. (B) Results of Sample 2. (C) Schematic picture of the size-sensitive aggregation and precipitation process when the temperature is increased above T_a. T_a is marked by vertical dotted lines in (A) to (B). Error bars represent one SD. Error bars may not be visible if they are smaller than symbols.

(red histogram) was around 5 nm with a long tail up to about 17 nm. This tail indicates the presence of large particles, the so-called ''impurities'', outside the expected normal (Gaussian) distribution at the main peak. The volume fraction contribution from these impurity particles was very significant in Sample 1. After purification at T_p = 31 °C (the black histogram in Fig. 5A) for Sample 1, the shape of the distribution resembles that of the normal distribution with a significant reduction in the peak position and its width. The main mode after the purification at T_p = 31 °C has an average value around 3.7 nm, and no particles larger than 6 nm were observed. A visual confirmation of the purification effect on Sample 1 can also be assessed from the AFM topographical images shown in Fig. 5C and D. In comparison with Sample 1, Sample 2 contains some P2 NPs besides P1 NPs. The addition of P2 NPs artificially introduces more impurities (large particles) into Sample 2. This can be seen in the range of large particle sizes of the

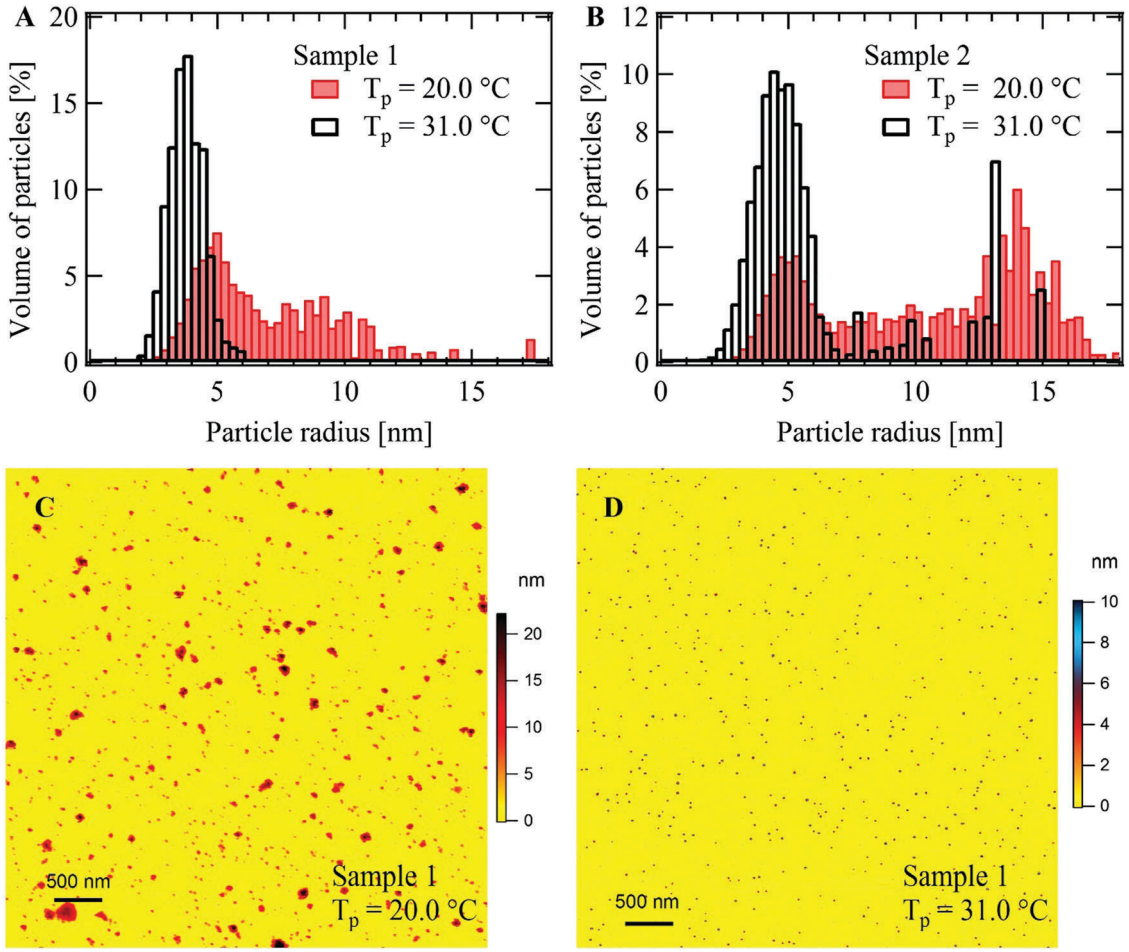

Fig. 5 Histograms of the volume distribution of the NPs as a function of the particle size collected from five independent AFM scans of the NPs on mica and AFM topographical images. (A) Histograms of Sample 1 at two temperatures show the particle size distributions before purification (T_p = 20 °C) and after the purification (T_p = 31 °C), respectively. (B) Histograms of Sample 2 show the particle size distribution before and after the purification. In (A) and (B) the bin size is 0.3 nm and the total numbers of the measured particles are larger than 2000 for each histogram. (C) One 5 μm × 5 μm AFM topographical image of Sample 1 (NPs on mica) before the purification, and there are many large particles present. (D) One AFM topographical image of Sample 1 after the purification at T_p = 31 °C, and there are no large particles.

histogram of Sample 2 before purification as shown in the red curve in Fig. 5B, which had significantly more particles larger than 10 nm. Similar to the Sample 1 case, the purification was very effective in removing most of the large particles after purifying Sample 2 at T_p = 31 °C (the black curve in Fig. 5B).

4. Conclusions

Combining the results from SANS, DLS, and AFM, we conclusively demonstrated here that the aggregation behavior induced by the CCF in our systems depends on the relative particle size of the samples for polydisperse systems. Since size polydispersity commonly exists in most colloidal systems, this observation provides important new physics insights into the widely studied colloidal stability problem in a binary solvent close to the solvent demixing temperatures.

The proposed particle size-selective process is demonstrated to be very efficient in separating small particles from larger ones. The large particles separated by this method can be either large impurities or potentially useful particles but needed to be removed from the solutions. By gradually changing T_p, larger particles in the solution aggregate, precipitate, and then can be separated from the supernatant step by step. As a result, a narrower distribution with a smaller average particle size can be obtained, similar to those shown in Fig. 3–5. With a detailed knowledge of the temperature dependence of the selective process, one can control the average particle size with high accuracy by varying T_p. Even though we used small-sized particles (a few nanometers) dispersed in a water/lutidine solvent to demonstrate the efficiency of our method, it has been shown that larger particles up to micrometers and other types of binary solvents with different types of NPs also have a phase behavior similar to the one shown in Fig. 1.[7,12] Thus, we believe that our method may also work for larger NPs and different binary solvents.

This purification method is very versatile. Even though the 1-phase with aggregations region is at the lutidine-rich side

($w > w_c$) for the current systems as our silica NPs favor water adsorption at particle surfaces, the same purification strategy may also work for NPs favoring lutidine on their surfaces. For such a case, the 1-phase with aggregations forms at the water-rich side ($w < w_c$) as shown in the literature.[7] Hence, to reach 1-phase with aggregations, the lutidine concentration should be smaller than w_c. We expect that the aggregation behavior will still depend on the size as the interaction force controlling the particle aggregation is still the CCF. Moreover, there are also other types of particles with different binary solvents showing aggregation behavior similar to our systems. It is thus also reasonable to hypothesize that the observed size-sensitive aggregation behavior and the NP purification strategy might still work for those systems even though more future experiments are needed to prove this.

The efficiency of this method relies on the CCF induced attraction between NPs. When changing the temperature, a solvent layer with more preferred solvent molecules forms on NP surfaces to induce the CCF between particles in a binary solvent. (In general, the surfaces of most colloidal particles in a binary solvent prefer one component over the other one. In fact, it is very difficult to make colloidal particles have an equal affinity for both components in a binary solvent.[32,33]) The attraction strength of the CCF can thus be very sensitively controlled by varying the solvent composition and the thickness of this solvent layer. (The thickness of the adsorption layer is related to the correlation length of the solvent fluctuation that can be sensitively controlled by the temperature.[5]) Further research efforts are still needed to determine the detailed criteria controlling the efficiency of the proposed purification method as the exact attraction strength induced by the CCF might also be affected by many other factors such as the charge density of NPs and the surface chemistry.[7,34,35]

Conflicts of interest

Some of the authors are the inventors of a U.S. patent filed by the University of Delaware related to the work presented here (Serial number 62/410,420).

Acknowledgements

Y. L. and H. Y. acknowledge the partial support of the Cooperative Agreement No. 70NANB12H239 and 70NANB10H256 of the National Institute of Standards and Technology (NIST), the U.S. Department of Commerce. Access to NGB 30m SANS was provided by the Center for High Resolution Neutron Scattering, a partnership between the National Institute of Standards and Technology and the National Science Foundation under Agreement No. DMR-1508249. The statements, findings, conclusions, and recommendations are those of the authors and do not necessarily reflect the view of NIST or the U.S. Department of Commerce. Identification of a commercial product does not imply recommendation or endorsement by NIST, nor does it imply that the product is necessarily the best for the stated purpose.

References

1 M. E. Fisher and P.-G. de Gennes, *C. R. Acad. Sci. Paris*, 1978, **t.287**(serie B), 207–209.
2 A. Hanke, F. Schlesener, E. Eisenriegler and S. Dietrich, *Phys. Rev. Lett.*, 1998, **81**, 1885–1888.
3 C. Hertlein, L. Helden, A. Gambassi, S. Dietrich and C. Bechinger, *Nature*, 2008, **451**, 172–175.
4 J. R. Edison, N. Tasios, S. Belli, R. Evans, R. van Roij and M. Dijkstra, *Phys. Rev. Lett.*, 2015, **114**, 38301.
5 C. E. Bertrand, P. D. Godfrin and Y. Liu, *J. Chem. Phys.*, 2015, **143**, 84704.
6 D. Beysens and D. Estève, *Phys. Rev. Lett.*, 1985, **54**, 2123–2126.
7 P. D. Gallagher, M. L. Kurnaz and J. V. Maher, *Phys. Rev. A: At., Mol., Opt. Phys.*, 1992, **46**, 7750–7755.
8 D. Bonn, J. Otwinowski, S. Sacanna, H. Guo, G. Wegdam and P. Schall, *Phys. Rev. Lett.*, 2009, **103**, 156101.
9 T. F. Mohry, S. Kondrat, A. Maciołek and S. Dietrich, *Soft Matter*, 2014, **10**, 5510.
10 V. D. Nguyen, M. T. Dang, T. A. Nguyen and P. Schall, *J. Phys.: Condens. Matter*, 2016, **28**, 43001.
11 T. W. Burkhardt and E. Eisenriegler, *Phys. Rev. Lett.*, 1995, **74**, 3189–3192.
12 Y. Jayalakshmi and E. W. Kaler, *Phys. Rev. Lett.*, 1997, **78**, 1379–1382.
13 S. Buzzaccaro, J. Colombo, A. Parola and R. Piazza, *Phys. Rev. Lett.*, 2010, **105**, 198301.
14 R. Okamoto and A. Onuki, *Phys. Rev. E: Stat., Nonlinear, Soft Matter Phys.*, 2013, **88**, 22309.
15 M.-C. Daniel and D. Astruc, *Chem. Rev.*, 2004, **104**, 293–346.
16 J. N. Anker, W. P. Hall, O. Lyandres, N. C. Shah, J. Zhao and R. P. Van Duyne, *Nat. Mater.*, 2008, **7**, 442–453.
17 E. Armstrong and C. O'Dwyer, *J. Mater. Chem. C*, 2015, **3**, 6109–6143.
18 J. D. Robertson, L. Rizzello, M. Avila-Olias, J. Gaitzsch, C. Contini, M. S. Magoń, S. A. Renshaw and G. Battaglia, *Sci. Rep.*, 2016, **6**, 27494.
19 B. Kowalczyk, I. Lagzi and B. A. Grzybowski, *Curr. Opin. Colloid Interface Sci.*, 2011, **16**, 135–148.
20 K. Park, H. Koerner and R. a. Vaia, *Nano Lett.*, 2010, **10**, 1433–1439.
21 O. Akbulut, C. R. MacE, R. V. Martinez, A. a. Kumar, Z. Nie, M. R. Patton and G. M. Whitesides, *Nano Lett.*, 2012, **12**, 4060–4064.
22 J. Lee, S. I. Stoeva and C. A. Mirkin, *J. Am. Chem. Soc.*, 2006, **128**, 8899–8903.
23 M. J. Hollamby, J. Eastoe, A. Chemelli, O. Glatter, S. Rogers, R. K. Heenan and I. Grillo, *Langmuir*, 2010, **26**, 6989–6994.
24 W. Zhao, L. Lin and I.-M. Hsing, *Langmuir*, 2010, **26**, 7405–7409.
25 C.-L. Wang, M. Fang, S.-H. Xu and Y.-P. Cui, *Langmuir*, 2010, **26**, 633–638.
26 P. G. de Gennes, *Rev. Mod. Phys.*, 1985, **57**, 827–863.

27 C. a Grattoni, R. a Dawe, C. Y. Seah and J. D. Gray, *J. Chem. Eng. Data*, 1993, **38**, 516–519.
28 B. Rathke, H. Grüll and D. Woermann, *J. Colloid Interface Sci.*, 1997, **192**, 334–337.
29 A.-C. Genix and J. Oberdisse, *Curr. Opin. Colloid Interface Sci.*, 2015, **20**, 293–303.
30 M. Kotlarchyk and S.-H. Chen, *J. Chem. Phys.*, 1983, **79**, 2461.
31 I. A. Rahman and V. Padavettan, *J. Nanomater.*, 2012, **2012**, 132424.
32 K. Stratford, *Science*, 2005, **309**, 2198–2201.
33 E. M. Herzig, K. A. White, A. B. Schofield, W. C. K. Poon and P. S. Clegg, *Nat. Mater.*, 2007, **6**, 966–971.
34 D. J. Plazek, *J. Phys. Chem.*, 1965, **69**, 3480–3487.
35 C. M. Ellis, *J. Chem. Educ.*, 1967, **44**, 405.

